Applied Surface Science 586 (2022) 152690

Contents lists available at ScienceDirect

Applied Surface Science

journal homepage: www.elsevier.com/locate/apsusc

Full Length Article

Perfluoropentacene thin films on Au(1 1 1) surfaces: Effect of kinetic energy and vibrational properties

Adem Yavuz [a,b], M. Fatih Danışman [a,c,*]

[a] Micro and Nanotechnology Department, Middle East Technical University, Ankara 06800, Turkey
[b] Center for Materials Research, Integrated Research Centers, Izmir Institute of Technology, Urla İzmir 35430, Turkey
[c] Department of Chemistry, Middle East Technical University, Ankara 06800, Turkey

ARTICLE INFO

Keywords:
Perfluoropentacene
Supersonic molecular beam deposition
Carboranethiol
Scanning
Nearfield Optical Microscopy

ABSTRACT

We studied vibrational properties and the effect of beam kinetic energy on perfluoropentacene (PFP) thin films grown by supersonic molecular beam deposition (SMBD) technique on gold surfaces. Though similar growth mechanism was observed for different beam kinetic energies, in the case of low coverage (less than 1 monolayer) films and for low deposition rates significant differences were observed in the properties of films grown by using helium and argon carrier gasses with the former case resulting in higher average grain size. For multilayer films however there were no significant differences between helium and argon grown films. Vibrational properties were investigated by using Infrared Scattering-type Scanning Nearfield Optical Microscopy (s-SNOM) on clean and m-carborane-1-thiol (M1) coated template-stripped gold (TSAu) substrates. For both substrates thick PFP films (15 nm) had similar spectra whereas there were significant differences in the spectra of thin films (1 nm) due to PFP-substrate interactions. Davydov splitting of the IR modes were observed for both 1 nm and 15 nm films indicating similar molecular arrangements in both type of films.

1. Introduction

Organic semiconductors (OSs) continue to enjoy intense research efforts due to their promising properties and advantages over their inorganic counterparts in electronic device applications, such as light-emitting diodes (LEDs), thin-film transistors (TFTs), and photovoltaic cells (PVCs).[1-5] Most molecular adsorption studies have focused on a few layers of OSs on different types of substrates in which molecule–molecule and molecule–substrate interactions are dominant.[3,5-12] These layers govern the interface properties and hence control charge carrier injection efficiencies along with other electronic properties. [9,13] Within these layers, molecules are arranged with two types of packing; herringbone and π-stacking. While the herringbone arrangement in OS crystal structure exhibits high charge mobilities, these values increase further with the π-stacking. [6] Controlling the molecular orientation in OS thin films and gaining an understanding of film growth mechanisms play an essential role in designing organic electronic devices with improved performance.

Perfluoropentacene (PFP) is composed of five linearly arranged benzene rings, terminated with F atoms.[14-16] Contrary to its cousin, pentacene (PEN), PFP is an n-type organic semiconductor and acts as a donor. While PFP-PEN heterostructures on metal surfaces have been studied heavily[7,13,17-22], growth mechanism of pure PFP films have not been investigated thoroughly.[11,16,23-28] However, for improving the device performance, understanding and controlling the OS-metal interface is very crucial. For instance, increasing the grain size was shown to improve the electron mobility in PFP thin film transistors. [29] In addition, ionization energy of OS-metal interface depends on the orientation of OS molecules and was shown to increase when PFP orientation changes from lying down to standing up on the surface. [1,3,5] On clean metal surfaces PFP molecules assemble in a lying-down π-stacking structure in the monolayer whereas they form a herringbone structure in the multilayer. [16,18,22,25,26,30,31] To control the orientation and other properties of OS monolayer films on metal surfaces several strategies have been utilized. Engstrom and coworkers [32] have employed different organic self-assembled monolayers (SAMs) on Au surfaces and were able to grow standing up PFP monolayer films whose island density strongly depended on the terminal group (surface energy) of the employed SAM. In addition, they were able to control island density by tuning the deposition rate **(DR)** which is a common approach in organic film growth by vacuum thermal evaporation.[33-35] Supersonic molecular beam deposition (SMBD) was demonstrated as

* Corresponding author.
E-mail address: danisman@metu.edu.tr (M. Fatih Danışman).

https://doi.org/10.1016/j.apsusc.2022.152690
Received 6 October 2021; Received in revised form 27 January 2022; Accepted 28 January 2022
Available online 9 February 2022

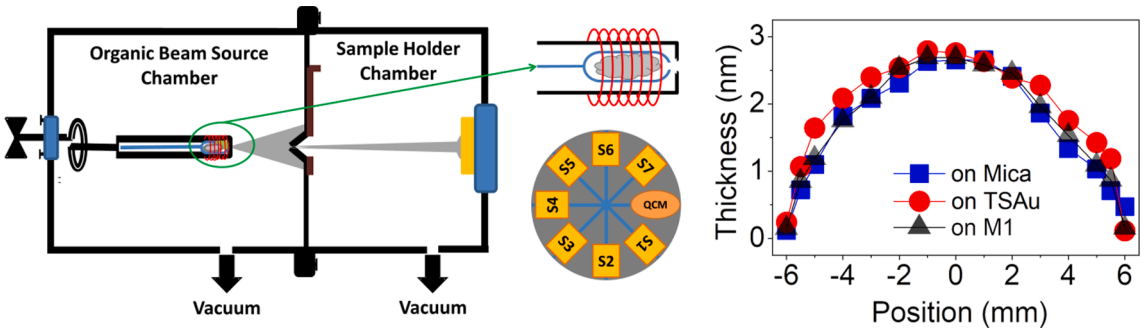

Fig. 1. Schematic diagrams of supersonic molecular beam deposition system (left), organic beam source used (middle-top) and the sample holder with QCM (middle-bottom). Local thickness of the films as a function of distance from the film center (film profile) is shown (right). Figure retrieved from [40].

Table 1
SMBD source working parameters during PFP film growth.

Carrier Gase	He	Ar
Nozzle Diameter (μm)	150	150
Stagnation Pressure (bar)	0.25	0.25
Evaporation Temperature (°C)	320 ± 10	340 ± 10
Nozzle Temperature (°C)	175 ± 10	175 ± 10
Kinetic Energy (eV)	12.8	1.28

another approach to improve film quality in OS monolayers by controlling the kinetic energy of the deposited organic molecules during film growth. By using this technique, improved TFT performance and film quality was shown for PEN films.[36-39] Recently, we reported PFP film growth by SMBD on surfaces with different hydrophobicities and showed mean grain size and dendricity of the PFP monolayer film to increase with decreasing deposition rate and increasing hydrophobicity of the substrate.[40]

Here, we report the effect of kinetic energy on the nucleation and growth mechanism of PFP films on template stripped gold (TSAu) surface. We used SMBD technique to tune the kinetic energy of PFP molecules and studied the resulting films by contact angle measurements and atomic force microscopy. We also provide scattering-type scanning near-field optical measurements (s-SNOM) of PFP films on TSAu and m-carborane-1-thiol SAM coated TSAu (M1) surfaces with the aim of providing insight to the vibrational properties of PFP films which so far have sparsely been studied only by conventional techniques.[41,42]

2. Experimental section

2.1. Substrate Preparation

Template-stripped gold (TSAu) and m-carborane-1-thiol self-assembled monolayers on TSAu (M1) were used as substrates. TSAu films were produced by following the procedures described before.[40,43] M1 substrates were obtained by keeping TSAu films in 1 mM ethanolic solution of m-carborane-1-thiol (Purchased from Katchem spol. s r.o., Czech Republic and used as received) all day long at room temperature. After taking off the substrates from the solution, the rinsing and drying processes were carried out with ethanol and N_2 stream, consecutively. Morphological and electronic properties of these substrates were reported before [40] and their roughness values were reported as 0.2 nm (for TSAu) and 0.4 nm (for M1).

2.2. PFP thin-film Preparation

The SMBD system consists of two high vacuum chambers separated by a shutter in front of the skimmer. These are the organic beam source (OBS) chamber in which PFP molecules are evaporated, and the sample holder chamber (SH) in which substrates and quartz crystal microbalance reside. High-capacity diffusion pumps pump each vacuum chamber and their operation pressures are P_{SH}: 5×10^{-6} Torr and P_{OBS}: 1×10^{-5} Torr. A schematic representation of the SMBD system used in this study is given in Fig. 1.

The source chamber consists of a Pyrex tube with hundreds of microns diameter hole, and in this pyrex tube, a quartz spoon (which will be referred to as source) containing the organic molecule is enclosed. The spiral heater causes the organic material placed in the source to evaporate in the flow of a carrier gas (usually helium, argon, or krypton). Evaporated molecules in the quartz tube mix with the carrier gas and the resulting mixture expands supersonically into the vacuum. During the production of a supersonic organic beam, the source and nozzle temperatures are controlled. Substrates and QCM on a moving mechanism can be inserted into and removed from the beam path. In the first step, the QCM is taken to the beam path and the flux of the material (deposition rate) to be grown in the beam is measured. Then the sample

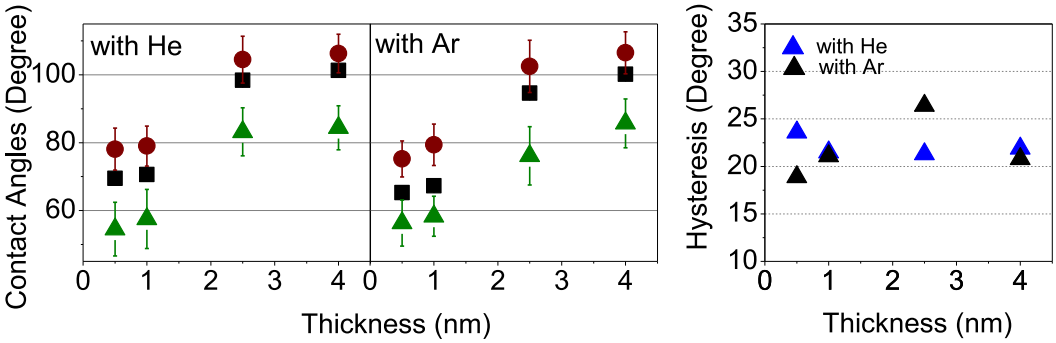

Fig. 2. Contact angle values of PFP films grown with He and Ar carrier gas with a nominal deposition rate of 0.025 Å/s vs. nominal film thickness measured by QCM. Static (black-square), advancing (red-circle) and receding (green-triangle) and hysteresis (blue and black triangle) are plotted. (For interpretation of the references to colour in this figure legend, the reader is referred to the web version of this article.)

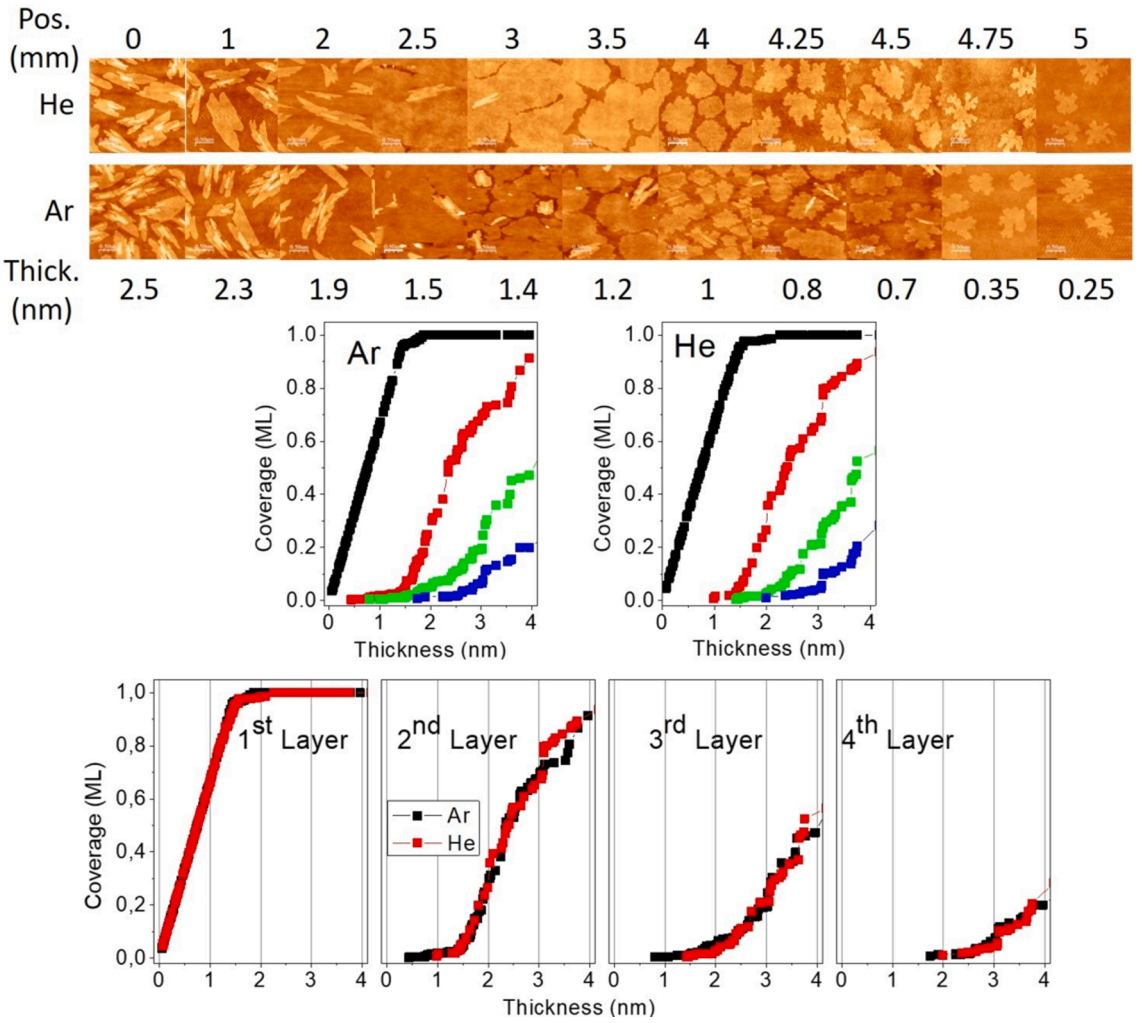

Fig. 3. Atomic force micrographs, 2.5x2.5 μm^2, of 2.5 nm nominal thickness PFP thin films (top). For both He and Ar grown films images were recorded at different positions from the film center (Pos.). Corresponding effective thicknesses values (Thick.) are also provided in the figure. Coverage vs. Thickness plots obtained by combining effective thicknesses data extracted from different nominal thickness films.

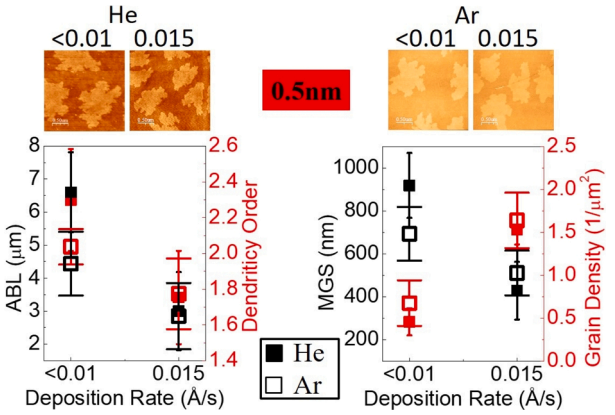

Fig. 4. AFM images (top) and grain size analysis (bottom) results for 0.5 nm (DR: 0.015 and lower than 0.01 Å/s) PFP films with carrier gases He (solid square), and Ar (open square).

(substrate) is inserted into the beam path, and the film growth process continues until the desired thickness film is obtained (by monitoring deposition time). By varying the source temperature and/or the pressure of the carrier gas, the flux and kinetic energy of the organic matter in the beam can be controlled. In addition, the speed (kinetic energy) of the organic matter in the beam can be increased by raising the temperature of the micro-nozzle and/or reducing the mass of the carrier gas (for example using helium instead of argon). Kinetic energy due to the supersonic expansion of the molecules in the lighter carrier gas can be estimated by the following equation:

$$E_{kin} = \frac{5}{2}\frac{m_{organic}}{m_{average}} RT_{Nozzle} \quad (1)$$

where E_{kin} is the kinetic energy; T_{nozzle} is the nozzle temperature; R is the gas constant; and m_{organic} and m_{average} are the molar mass of the organic molecule and average molar mass, respectively. In our previous studies with PEN [36,44], under the standard SMBD working conditions, kinetic energies were measured by time of flight measurements for both He and Kr carrier gases (2.2 eV and 0.2 eV for He and Kr, respectively) and these results were in the same range with those calculated by eqn. (1) (5 eV and 0.4 eV for He and Kr, respectively). [39] The SMBD source parameters employed in this study for the growth of PFP are summarized in Table 1. For tuning the PFP kinetic energy two different carrier gases (He and Ar) were used while keeping the nozzle temperature constant. By assuming infinite dilution, the upper limit for the kinetic energy of PFP molecules can be calculated to change from 12.8 eV to 1.28 eV by changing the carrier gas from He to Ar, respectively.

The area on the substrate covered by the film can be controlled by

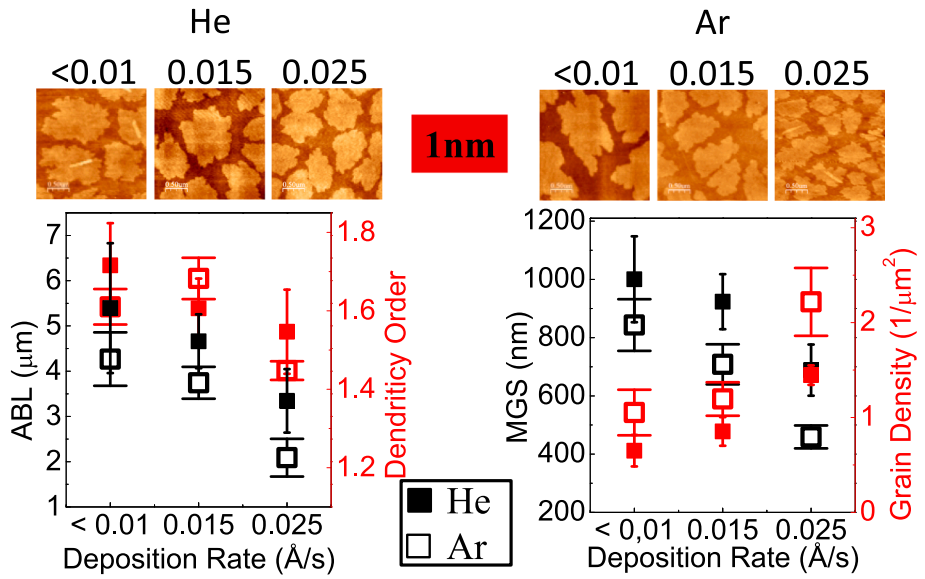

Fig. 5. AFM images (top) and grain size analysis (bottom) results for 1 nm (DR: 0.025, 0.015 and lower than 0.01 Å/s) PFP films with carrier gases He (solid square), and Ar (open square).

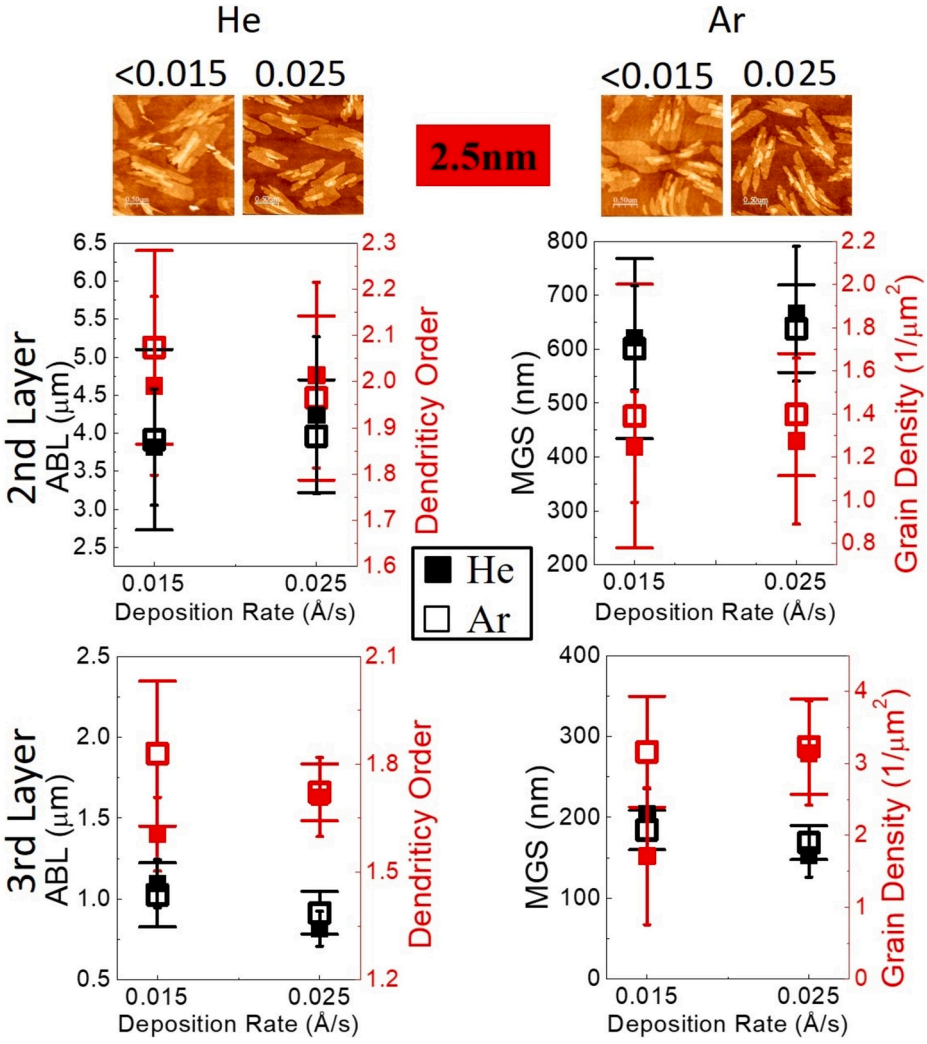

Fig. 6. AFM images (top) and grain size analysis (bottom) results for 2.5 nm (DR: 0.025, 0.015 Å/s) PFP films with carrier gases He (solid square), and Ar (open square) for 2nd and 3rd layers.

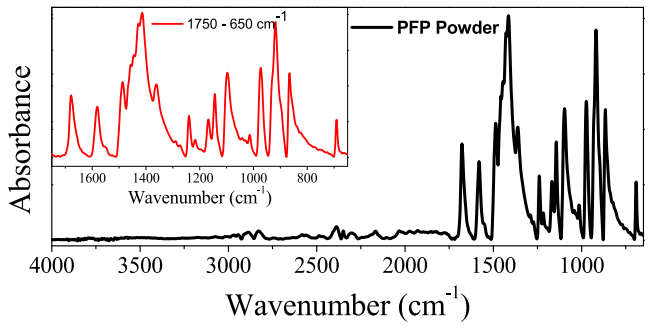

Fig. 7. ATR absorption spectrum of PFP powder recorded with a scan number of 128 per run at a resolution of 2 cm^{-1}.

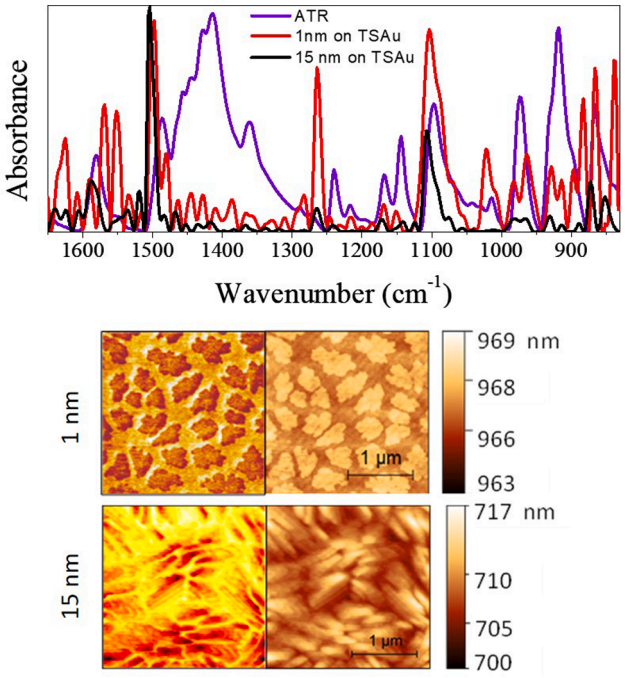

Fig. 8. Absorption spectra (top row) and SNOM absorption amplitude (bottom left) and AFM height image (bottom right) for 1 nm and 15 nm PFP on TSAu.

changing the distance between the skimmer and the sample holder. In this study this distance was kept at 3 cm which results in a circular film with a diameter of about 12 mm. Effective (local) thickness values can be obtained by performing AFM analysis over 2.5 um × 2.5 um regions located at different distances from the film center which shows a Gaussion film profile with a central homogenous region of 5 mm diameter as shown in Fig. 1. The effective thickness values at the center of the film are in agreement with nominal thicknesses determined by QCM.

In this study, all the films were grown with a nominal deposition rate (DR) of 0.025 Å/s to study the effect of beam kinetic energy and 0.05 Å/s for investigating the vibrational properties of PFP thin films. The deposition rates given in the results part correspond to the effective deposition rates and the thicknesses given are the effective thicknesses (unless otherwise is explicitly mentioned). For each set of growth parameters at least 3 parallel samples (3 different samples with the same growth conditions) were prepared and data (contact angle and AFM) were collected from at least 3 different points on each sample.

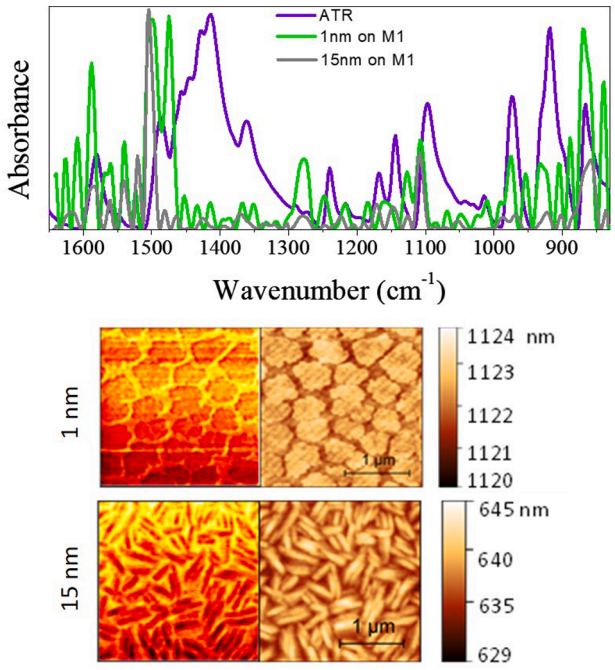

Fig. 9. Absorption spectra (top row) and SNOM absorption amplitude (bottom left) and AFM height image (bottom right) for 1 nm and 15 nm PFP on M1.

2.3. Contact angles

Static and dynamic contact angle measurements were performed with deionized water on an Attension Theta Lite optical tensiometer at room temperature. Water droplets of approximately 2.0 μL were placed on sample surfaces and a charge-coupled device (CCD) camera was used to capture the images at 20 frames per second, described in detail previously.[40,43] Recorded angles are subject to an error of ± 0.1°.

2.4. Atomic force Microscopy

AFM studies were performed with an Ambient AFM/MFM (Nanomagnetics instruments, Ankara). Contact mode measurements were performed by using Al coated silicon PPP-CONTR probes, in constant force mode with a set-point of 0.1 V. All measurements were performed in ambient air at room temperature. AFM images were processed by using Gwyddion software (version 2.53). All AFM imaging procedures were described in detail previously. [40]

2.5. Scattering-type Scanning Nearfield Optical Microscopy (s-SNOM)

Infrared Scattering-type Scanning Nearfield Optical Microscopy (s-SNOM) measurements were performed at Turkish Accelerator and Radiation Laboratory (TARLA) Experimental Stations in Ankara University, Institute of Accelerator Technologies. A s-SNOM setup (Neaspec Gmbh, Germany) equipped with a mid-IR DFG laser (average output power of about 600 μW) with wavelengths 5–15 μm was used in this work. Measurements were performed in tapping mode using a Pt coated AFM probe (NanoWorld Arrow NCPt) with a tapping frequency of ~ 250 kHz and a tapping amplitude of 60 nm. An AFM test grating (Si wafer) was used to obtain a reference spectrum before the chemical characterization of samples. Infrared near-field imaging and obtaining hyperspectral spectroscopy with chemical identification was performed by asymmetric Michelson interferometer. Full spectra were recorded from 2.5 μm × 2.5 μm region at 10.6 ms per pixel with a 2 cm^{-1} spectral resolution. The resulting interferograms were detected by a Mercury-Cadmium-Telluride (MCT) detector in the spectral range of 800–1700

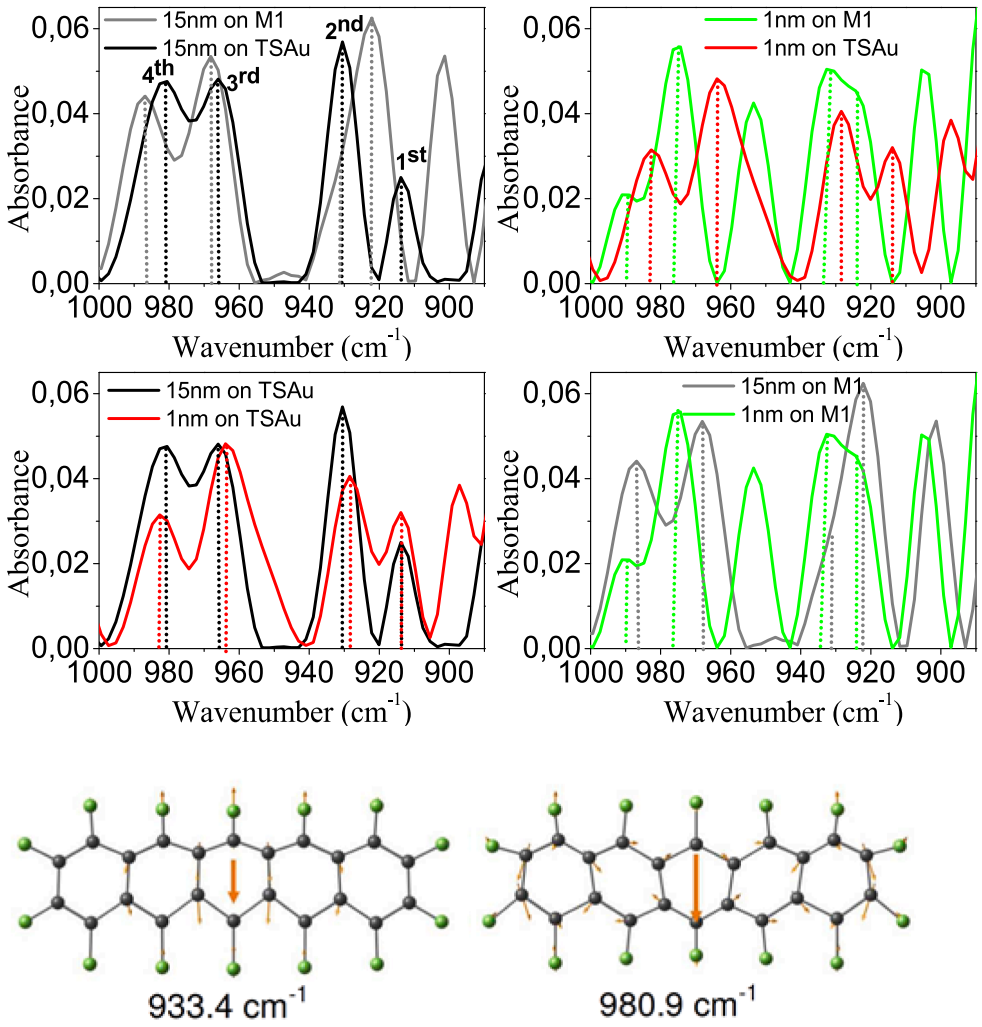

Fig. 10. Comparison of vibrational spectra of PFP films on TSAu and M1 in the region between 1000 and 890 cm^{-1} (top and middle rows). Schematic representation of characteristic C-F in-plane stretching modes(bottom row) as retrieved from [42].

cm^{-1} (Channel-B) with a spot size of approximately 50 nm (commercial value is about 20 nm and this value is directly depending on the tip curvature and sharpness). In our measurements, absorption amplitude images were taken from 3 parallel samples (3 different samples prepared with the same growth conditions) to assure reproducibility, and absorption spectra were extracted from 10 different points from each of these images. In the results sections representative spectra are shown.

3. Results and discussions

3.1. Contact angle measurements

CA values versus nominal film thickness are shown in Fig. 2, for PFP films grown with different carrier gases. For both carrier gases, static and dynamic CAs increase gradually with thickness and, after 2.5 nm, advancing CAs converge to about 110°, which indicates that after 2.5 nm thickness, TSAu surfaces are completely covered with PFP films. Though the contact angles for both types of films are very close to each other, which points to similar film morphologies, in the case of Ar carrier gas they are slightly lower suggesting minor differences in the film structure as will be discussed in the following section.

3.2. Grain analysis of kinetic energy effects on PFP films

In Fig. 3, AFM images and coverage vs. thickness plots for PFP films on TSAu grown by using He and Ar carrier gases are shown. Fig. 3 shows coverage versus thickness plots that were obtained by using AFM grain analysis from different nominal thickness films (1 nm, 2.5 nm, and 4 nm). Similar to what was observed in our previous study [40], the PFP growth follows a layer + island mechanism with different carrier gases as well, where the first layer completely wets substrate surface and second and other layers start to form needle-like grains on this first layer immediately. PFP films were reported to show similar behavior on other surfaces before. [1,32,40,45] For both carrier gases, the 2nd layers start to form even before 1st layer is completed. The grain shapes are also similar: 1st layer has circular grains and the overlayers' grains are more elongated/rectangular. Coverage-thickness plots show that each layer follows a similar growth mechanism for different kinetic energy (Fig. 3 bottom row). However, in the case of Ar gas, 2nd and higher-order layers start to grow sooner than those with He.

Grain size analysis for 0.5 nm thick films is provided in Fig. 4 for different deposition rates along with representative AFM images. As expected, as the deposition rate decreases, mean grain size (MGS) increases, and accordingly grain density decreases. [32,40,46-48] Grain density changes from 1.5 grains/μm^2 to 0.5 grains/μm^2, as DR, decreases from 0.015 to less than 0.01 Å/s for both gases which implies that carrier gas type does not affect grain density significantly. On the other hand, MGS, dendricity, and average boundary length (ABL) are significantly different for He and Ar when the DR is less than 0.01 Å/s. Such a difference, however, is not present for the DR of 0.015 Å /s. This

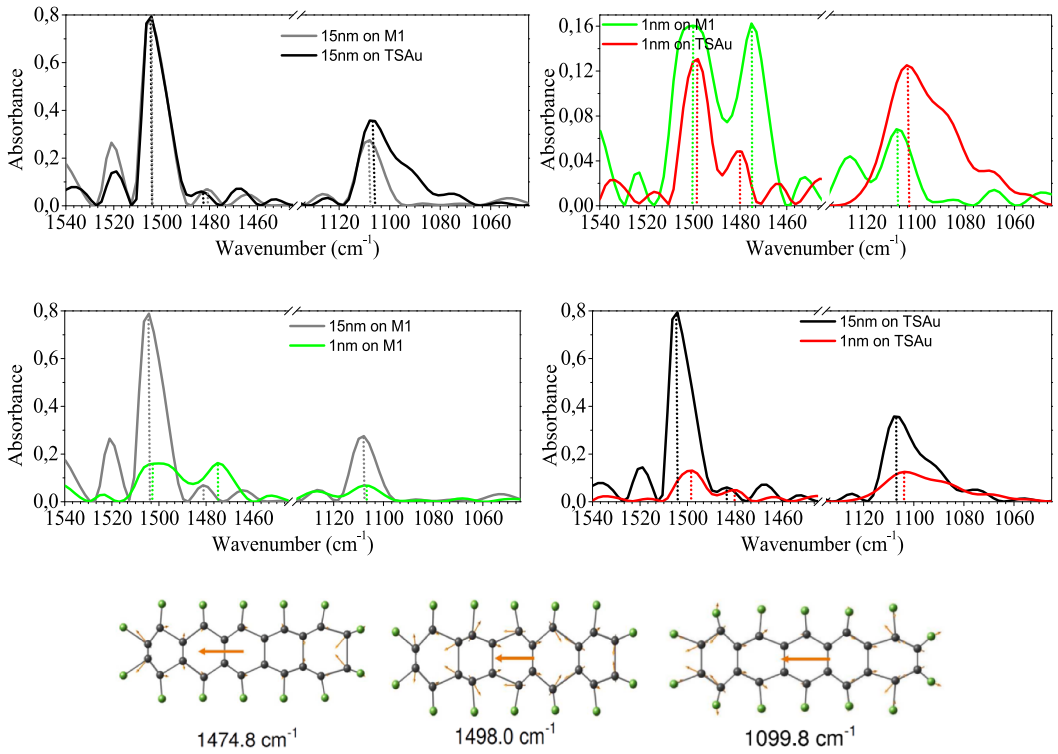

Fig. 11. Comparison of vibrational spectra of PFP films on TSAu and M1 in the region around 1500 cm^{-1} and 1100 cm^{-1} (top and middle rows). Schematic representation of vibrational modes around 1500 cm^{-1} and 1100 cm−1 (bottom row) as retrieved from [42].

finding implies that changing the kinetic energy of the PFP molecules results in a difference in the film properties only for low deposition rates. ABL, MGS and the dendriticy of grains increase as DR decreases for both gasses. However, the amount of increase is significantly larger for He: MGS values increased by 2.1 and 1.4 times, ABL values increased by 2.2 and 1.5 times and dendricity increased by 1.3 and 1.1 times for He and Ar, respectively. This observation indicates that film growth is affected by the DR more significantly when the carrier gas is lighter (kinetic energy is higher). Considering that the films obtained with both carrier gases are grown on the same substrate, this result shows that varying the carrier gas (hence beam kinetic energy) affects the film formation. Grain heights are similar for both carrier gases and are about 1.5 nm. This value is equal to the length of PFP molecules indicating standing up molecules on the substrate surface.

Grain size analysis and comparisons for 1 nm thick films as a function of DR and carrier gas are provided in Fig. 5 along with representative AFM images. Though carrier gas type doesn't affect grain density significantly, in the case of Ar, grain density remains a little higher than its He counterpart. As discussed above, grain shapes for the 1st layer are almost circular in both cases. As expected, dendriticy order increases, while DR decreases from 0.025 to less than 0.01 Å/s. As DR decreases, ABL and MGS values increase similarly for both He and Ar gases, and similar results have been seen in 0.5 nm films. However, for the same DRs, ABL and MGS values are higher for He than those for Ar. This could be directly related to the kinetic energy of the PFP molecular beam. [49] Because in the case of high kinetic energy, PFP molecules impinging the surface may have higher diffusion length on the surface, so they will have a higher probability to encounter nucleated clusters on the surface and tend to combine with those clusters to create larger grains more quickly. In contrast, PFP molecules impinging the surface with the low-energy state will form smaller grains on the substrate as the diffusion on the surface may be limited. For this reason, grain densities are higher (inversely MGSs are lower) in the low-energy state. In addition, the fact that static contact angle results for 0.5 nm and 1 nm films (see Fig. 2) are slightly higher in the case of high kinetic energy than in the case of low kinetic energy also indicates that the film formation is faster in the high energy state.

Fig. 6 shows the AFM images of 2.5 nm thick PFP films grown with different DRs and the corresponding grain size analysis for the 2nd and 3rd layers. In 2.5 nm thickness films, the 1st layer completely covers the substrate for both carrier gases, and the 2nd and higher layers form needle-like grains on this 1st layer. For both 2nd and 3rd layers, none of the analyzed parameters (ABL, dendricity, MGS, and grain density) change significantly with DR and carrier gas. This implies that in the DR and thickness range studied, multilayer film growth is insensitive to carrier gas type.

3.3. *Infrared Scattering-type Scanning Nearfield Optical Microscopy (s-SNOM) results of PFP thin-films*

Fig. 7 shows ATR spectra recorded for PFP powder to act as a reference for s-SNOM studies. PFP molecules exhibit very strong vibrational modes between 1750 and 650 cm^{-1}, indicating which region we need to focus on to determine the vibrational properties of PFP molecules. It can be clearly seen from the ATR results that the strong absorption modes are at around 1600 cm^{-1}, 1300–1500 cm^{-1}, 1250 cm^{-1}, 1100 cm^{-1}, and 1000–850 cm^{-1}. The peaks between 1000 and 850 cm^{-1} can be associated with PFP's characteristic C-F in-plane stretching modes. At 1250 cm^{-1} and 1100 cm^{-1}, PFP has C-F asymmetric and symmetric stretching modes, respectively. The peaks around 1500 cm^{-1} can be attributed to C = C stretching modes. Finally, the very broad peak between 1500 and 1250 cm^{-1} is due to the existence of water.

AFM/s-SNOM images and total absorption spectra of 1 nm and 15 nm PFP thin films grown on TSAu and M1 by using helium carrier gas with a deposition rate of 0.05 Å/s are given in Fig. 8 and Fig. 9. For comparison, ATR results of PFP powder are shown as well in total absorption spectra. The absorption peaks in the s-SNOM spectra can be seen to have shifted to higher energies than those in the ATR. In the thin-film phase, such shifts are understandable due to substrate-molecule interactions. [42] The absorption amplitude images can be considered to be analogous to

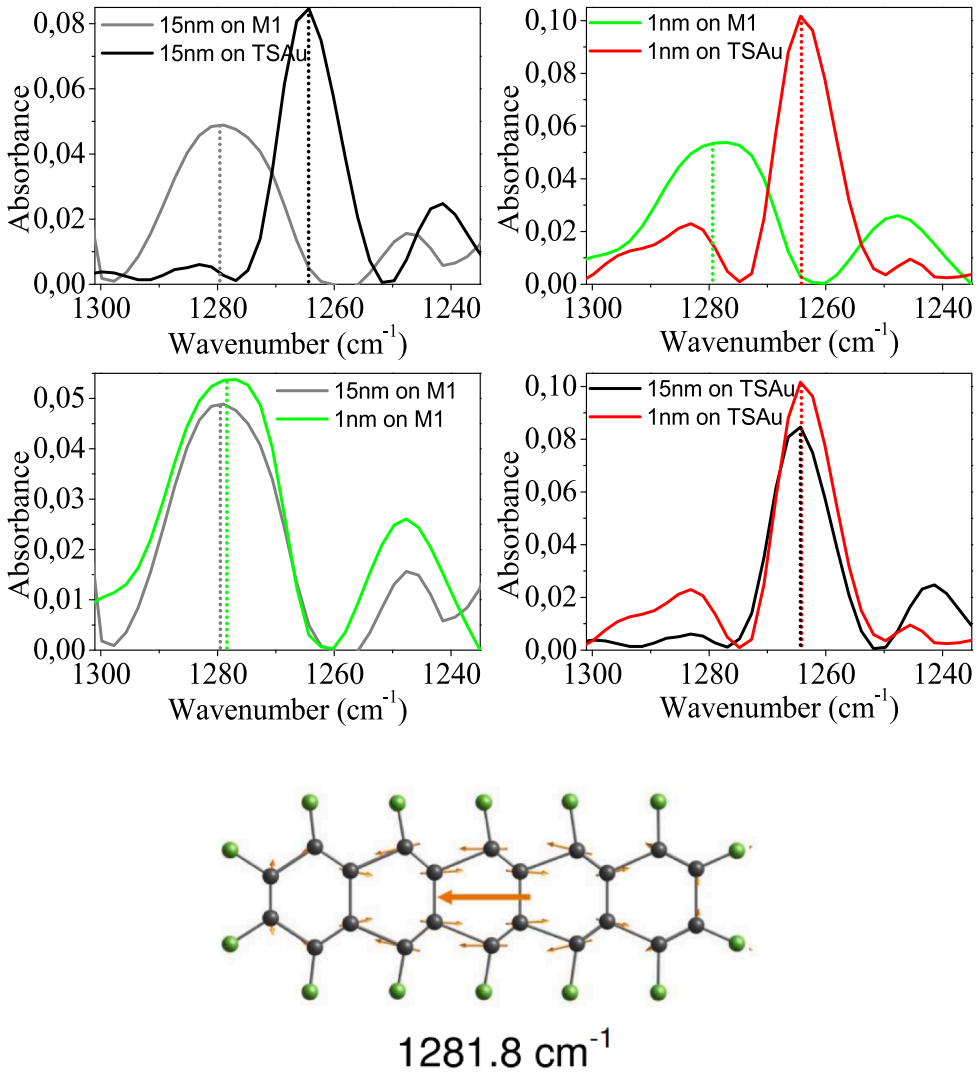

Fig. 12. Comparison of vibrational spectra of PFP films on TSAu and M1 in the region between 1300 and 1240 cm^{-1} (top and middle rows). Schematic representation of vibrational modes around 1280 cm^{-1} (bottom row) as retrieved from [42].

AFM phase images and the darker regions indicate IR active areas on the surface which correlate with the PFP covered parts (or island tops) visible in the AFM height images. Below, different regions of the IR spectra will be discussed in detail:

A comparison of characteristic C-F in-plane stretching modes on TSAu and M1 is given in Fig. 10. Based on theoretical calculations of PFP molecules, characteristic C-F/C-C in-plane stretching modes were reported to be at 920 (1st peak), 933 (2nd peak), 974 (3rd peak), and 980 (4th peak) cm^{-1}, in the literature. [15,42,50] Breuer et al. [42] showed that for PFP molecules adsorbed in lying flat configuration, with π-stacking, there are only two peaks arising between 1000 and 900 cm^{-1}; these results were confirmed by both experimental measurements and theoretical calculations. The single-molecule DFT calculations and π-stacking (PFP molecules absorb in lying down geometries) experimental results are compatible with each other, and peaks arise at 933 and 980 cm^{-1} (DFT results are given in Fig. 10). In the case there exist a second oriented species within the unit cell (as in herringbone packing), characteristic vibrational modes are split, known as Davydov splitting. In the study of Breuer et al., when the PFP molecules absorb in standing up geometries, these two characteristic peaks split and were observed at 920 (1st peak), 933 (2nd peak), 974 (3rd peak), and 980 (4th peak) cm^{-1}. This observation was explained to be a result of herringbone stacking arrangement in the crystal structure of PFP films.

Since our results show 4 peaks for both 1 nm and 15 nm films it can be concluded that the crystal structure for both thicknesses is similar with standing up molecules oriented in herringbone fashion. Nevertheless, there still exist some differences as will be discussed below: When the spectra of the identical thickness films on different substrates are compared (Fig. 10 top row) it can be seen that there is a larger difference between the 1 nm films which is most probably due to different substrate-molecule interactions. For 15 nm films, however, the spectra are pretty similar (especially for 3rd and 4th peaks) for different substrates. This is also expected since at this thickness the films show bulk-like properties regardless of the substrate. When spectra of different thickness films on the same substrate (Fig. 10 bottom row) are examined, on TSAu 1 nm and 15 nm films can be seen to have very similar structure apart from the low energy shoulder around 960 cm-1 peaks. For the films on M1 however, there is considerable change in the spectra with changing thickness.

A comparison of vibrational modes around 1500 cm^{-1} and 1100 cm^{-1} is shown in Fig. 11. For 15 nm films, the spectra recorded on M1 and TSAu are very similar due to bulk like the structure of the "thick" films (Fig. 11 top row) and there is a significant difference in the intensities and the positions of the peaks for 1 nm and 15 nm films (Fig. 11 bottom row). In the case of 1 nm films, spectra strongly change with changing substrate due to PFP-substrate interactions. For instance, for 1

nm film on M1, there is a strong peak at 1475 cm^{-1} while this peak has a much lower intensity and shifted to higher energy on TSAu. Finally, since all the peaks in these regions are associated with modes with transition dipole moments parallel to the long molecular axis, no Davydov splitting is observed.

C-F/C-C asymmetric stretching vibrational modes around 1270 cm^{-1} are shown in Fig. 12. [51] Interestingly the peak positions and intensities are almost identical for 15 nm and 1 nm films on both substrates with the position of 1264 cm^{-1} on TSAu and at 1279 cm^{-1} on M1 (Fig. 12 bottom row). In addition, peak profiles are significantly different for different substrates even in the case of 15 nm films (Fig. 12 top row). This behavior is the opposite of what have been observed for the other regions discussed above.

4. Conclusion:

Coverage-thickness plots evolve quite similarly for both carrier gases after the completion of the 1st layer and indicate a layer plus island (Stranski–Krastanow) growth mode. In the case of Ar gas, the 2nd and 3rd layer start to grow on the TSAu surface sooner than those of He. Considering the contact angle measurement results, it can be concluded that TSAu substrates, up to 2.5 nm PFP film thickness, are not covered completely and the CA values are relatively higher in the case of high kinetic energy (carrier gas He), which shows that the film formation is faster in the high kinetic energy state. Although the film formation mechanism seems similar for both gases it is clear that ABL, dendricity, MGS (and grain density inversely proportional to MGS) values are much higher for He when compared with Ar for low coverage films. As DR decreases, ABL and MGS values increase similarly for both He and Ar gases. Grain heights are also similar for both carrier gases and are about 1.5 nm and indicate that the molecules are standing up along their long axis on the substrate. s-SNOM results indicate that molecular arrangement (packing) in PFP films is similar for both thin-film and bulk phase with the herringbone arrangements evidenced by the Davydov splitting. The shifts in 1 nm films compared to 15 nm films, points to a different molecular environment of PFP molecules, which could be attributed to strong intermolecular interactions between PFP molecules and substrates.

CRediT authorship contribution statement

Adem Yavuz: Investigation, Methodology, Formal analysis, Writing – original draft. **M. Fatih Danışman:** Conceptualization, Methodology, Supervision, Writing – review & editing.

Declaration of Competing Interest

The authors declare that they have no known competing financial interests or personal relationships that could have appeared to influence the work reported in this paper.

Acknowledgments

This work was supported by TÜBİTAK Grant no. 113F022 and partially supported by Middle East Technical University BAP Grant no. DKT-103-2018-3683. We thank Turkish Accelerator and Radiation Laboratory for s-SNOM measurements.

References

[1] N. Koch, Electronic structure of interfaces with conjugated organic materials, Phys. Status Solidi - Rapid Res. Lett. 6 (7) (2012) 277–293, https://doi.org/10.1002/pssr.201206208.
[2] O.M. Cabarcos, S. Schuster, I. Hehn, P.P. Zhang, M.M. Maitani, N. Sullivan, J.-B. Giguère, J.-F. Morin, P.S. Weiss, E. Zojer, M. Zharnikov, D.L. Allara, Effects of Embedded Dipole Layers on Electrostatic Properties of Alkanethiolate Self-Assembled Monolayers, J. Phys. Chem. C. 121 (29) (2017) 15815–15830, https://doi.org/10.1021/acs.jpcc.7b0469410.1021/acs.jpcc.7b04694.s001.
[3] Q. Wang, M.T. Chen, A. Franco-Cañellas, B. Shen, T. Geiger, H.F. Bettinger, F. Schreiber, I. Salzmann, A. Gerlach, S. Duhm, Impact of fluorination on interface energetics and growth of pentacene on Ag(111), Beilstein J. Nanotechnol. 11 (2020) 1361–1370, https://doi.org/10.3762/BJNANO.11.120.
[4] M. Fahlman, S. Fabiano, V. Gueskine, D. Simon, M. Berggren, X. Crispin, Interfaces in organic electronics, Nat. Rev. Mater. 4 (10) (2019) 627–650, https://doi.org/10.1038/s41578-019-0127-y.
[5] G. Heimel, I. Salzmann, S. Duhm, N. Koch, Design of organic semiconductors from molecular electrostatics, Chem. Mater. 23 (3) (2011) 359–377, https://doi.org/10.1021/cm1021257.
[6] I. Salzmann, A. Moser, M. Oehzelt, T. Breuer, X. Feng, Z.-Y. Juang, D. Nabok, R. G. Della Valle, S. Duhm, G. Heimel, A. Brillante, E. Venuti, I. Bilotti, C. Christodoulou, J. Frisch, P. Puschnig, C. Draxl, G. Witte, K. Müllen, N. Koch, Epitaxial growth of π-stacked perfluoropentacene on graphene-coated quartz, ACS Nano. 6 (12) (2012) 10874–10883, https://doi.org/10.1021/nn3042607.
[7] N. Koch, A. Gerlach, S. Duhm, H. Glowatzki, G. Heimel, A. Vollmer, Y. Sakamoto, T. Suzuki, J. Zegenhagen, J.P. Rabe, F. Schreiber, Adsorption-induced intramolecular dipole: Correlating molecular conformation and interface electronic structure, J. Am. Chem. Soc. 130 (23) (2008) 7300–7304, https://doi.org/10.1021/ja800286k.
[8] E. Empting, M. Klopotek, A. Hinderhofer, F. Schreiber, M. Oettel, Lattice gas study of thin-film growth scenarios and transitions between them: Role of substrate, Phys. Rev. E. 103 (2021) 23302, https://doi.org/10.1103/PhysRevE.103.023302.
[9] S. Smalley, P. Darancet, J.R. Guest, J.A. Smerdon, Monolayer and Bilayer Perfluoropentacene on Cu(111), J. Phys. Chem. C. 124 (1) (2020) 653–658, https://doi.org/10.1021/acs.jpcc.9b0967010.1021/acs.jpcc.9b09670.s001.
[10] B. Bräuer, R. Kukreja, A. Virkar, H.B. Akkerman, A. Fognini, T. Tyliszczak, Z. Bao, Carrier mobility in pentacene as a function of grain size and orientation derived from scanning transmission X-ray microscopy, Org. Electron. 12 (11) (2011) 1936–1942, https://doi.org/10.1016/j.orgel.2011.08.007.
[11] N. Koch, N. Ueno, A.T.S. Wee, The Molecule-Metal Interface, Wiley-VCH, Singapore (2013), https://doi.org/10.1002/9783527653171.
[12] W. Zhang, J.R. Engstrom, Effect of substrate composition on atomic layer deposition using self-assembled monolayers as blocking layers, J. Vac. Sci. Technol. A Vacuum, Surfaces, Film. 34 (1) (2016) 01A107, https://doi.org/10.1116/1.4931722.
[13] Q.i. Wang, J. Yang, A. Franco-Cañellas, C. Bürker, J. Niederhausen, P. Dombrowski, F. Widdascheck, T. Breuer, G. Witte, A. Gerlach, S. Duhm, F. Schreiber, Pentacene/perfluoropentacene bilayers on Au(111) and Cu(111): Impact of organic-metal coupling strength on molecular structure formation, Nanoscale Adv. 3 (9) (2021) 2598–2606.
[14] F. Rocio, Electron Microscopy Characterization of Pentacene and Perfluoropentacene Grown on Different Substrates, Philipps-Universitat Marburg, 2017. https://doi.org/https://doi.org/10.17192/z2017.0541.
[15] I. Salzmann, S. Duhm, G. Heimel, J.P. Rabe, N. Koch, M. Oehzelt, Y. Sakamoto, T. Suzuki, Structural order in perfluoropentacene thin films and heterostructures with pentacene, Langmuir. 24 (14) (2008) 7294–7298, https://doi.org/10.1021/la800606h.
[16] C. Schmidt, T. Breuer, S. Wippermann, W.G. Schmidt, G. Witte, Substrate induced thermal decomposition of perfluoro-pentacene thin films on the coinage metals, J. Phys. Chem. C. 116 (45) (2012) 24098–24106, https://doi.org/10.1021/jp307316r.
[17] A.-K. Hansmann, R.C. Döring, A. Rinn, S.M. Giesen, M. Fey, T. Breuer, R. Berger, G. Witte, S. Chatterjee, Charge transfer excitation and asymmetric energy transfer at the interface of pentacene-perfluoropentacene heterostacks, ACS Appl. Mater. Interfaces. 13 (4) (2021) 5284–5292, https://doi.org/10.1021/acsami.0c1617210.1021/acsami.0c16172.s001.
[18] N. Koch, A. Vollmer, S. Duhm, Y. Sakamoto, T. Suzuki, The effect of fluorination on pentacene/gold interface energetics and charge reorganization energy, in, Adv. Mater., Wiley-Blackwell 19 (1) (2007) 112–116, https://doi.org/10.1002/adma.200601825.
[19] L. von Helden, T. Breuer, G. Witte, Anisotropic thermal expansion in pentacene and perfluoropentacene: Effects of molecular packing motif and fixation at the interface, Appl. Phys. Lett. 110 (14) (2017) 141904, https://doi.org/10.1063/1.4979650.
[20] R. Félix, T. Breuer, G. Witte, K. Volz, K.I. Gries, Microstructural study of codeposited pentacene:perfluoropentacene grown on KCl by TEM techniques, J. Cryst. Growth. 471 (2017) 29–36, https://doi.org/10.1016/J.JCRYSGRO.2017.05.009.
[21] S.L. Wong, H. Huang, Y.L. Huang, Y.Z. Wang, X.Y. Gao, T. Suzuki, W. Chen, A.T. S. Wee, Effect of fluorination on the molecular packing of perfluoropentacene and pentacene ultrathin films on Ag (111), J. Phys. Chem. C. 114 (20) (2010) 9356–9361, https://doi.org/10.1021/jp910581b.
[22] Y.-Y. Lo, J.-H. Chang, G. Hoffmann, W.-B. Su, C.-I. Wu, C.-S. Chang, A Comparative Study on the Adsorption Behavior of Pentacene and Perfluoropentacene Molecules on Au (111) Surfaces, Jpn. J. Appl. Phys. 52 (10R) (2013) 101601, https://doi.org/10.7567/JJAP.52.101601.
[23] M. Marks, C. Schmidt, C.H. Schwalb, T. Breuer, G. Witte, U. Höfer, Temperature dependent structural phase transition at the perfluoropentacene/Ag(111) interface, J. Phys. Chem. C. 116 (2) (2012) 1904–1911, https://doi.org/10.1021/jp2094577.
[24] J. Götzen, C.H. Schwalb, C. Schmidt, G. Mette, M. Marks, U. Höfer, G. Witte, Structural evolution of perfluoro-pentacene films on Ag(111): Transition from 2D to 3D growth, Langmuir. 27 (3) (2011) 993–999, https://doi.org/10.1021/la1022664.

[25] S. Duhm, S. Hosoumi, I. Salzmann, A. Gerlach, M. Oehzelt, B. Wedl, T.-L. Lee, F. Schreiber, N. Koch, N. Ueno, S. Kera, Influence of intramolecular polar bonds on interface energetics in perfluoro-pentacene on Ag(111), Phys. Rev. B - Condens. Matter Mater. Phys. 81 (4) (2010), https://doi.org/10.1103/PhysRevB.81.045418.
[26] H. Glowatzki, G. Heimel, A. Vollmer, S.L. Wong, H. Huang, W. Chen, A.T.S. Wee, J. P. Rabe, N. Koch, Impact of fluorination on initial growth and stability of pentacene on Cu(111), J. Phys. Chem. C. 116 (14) (2012) 7726–7734, https://doi.org/10.1021/jp208582z.
[27] D.G. de Oteyza, Y. Wakayama, X. Liu, W. Yang, P.L. Cook, F.J. Himpsel, J. E. Ortega, Effect of fluorination on the molecule-substrate interactions of pentacene/Cu(1 0 0) interfaces, Chem. Phys. Lett. 490 (1-3) (2010) 54–57, https://doi.org/10.1016/j.cplett.2010.03.006.
[28] K. Toyoda, I. Hamada, S. Yanagisawa, Y. Morikawa, Density-functional theoretical study of fluorination effect on organic/metal interfaces, Org. Electron. Physics, Mater. Appl. 12 (2) (2011) 295–299, https://doi.org/10.1016/j.orgel.2010.11.010.
[29] Y. Inoue, Y. Sakamoto, T. Suzuki, M. Kobayashi, Y. Gao, S. Tokito, Organic Thin-Film Transistors with High Electron Mobility Based on Perfluoropentacene, Jpn. J. Appl. Phys. 44 (6A) (2005) 3663–3668, https://doi.org/10.1143/JJAP.44.3663.
[30] T. Breuer, G. Witte, Controlling nanostructures by templated templates: Inheriting molecular orientation in binary heterostructures, ACS Appl. Mater. Interfaces. 7 (36) (2015) 20485–20492, https://doi.org/10.1021/acsami.5b07409.
[31] H. Yang, T.J. Shin, M.-M. Ling, K. Cho, C.Y. Ryu, Z. Bao, Conducting AFM and 2D GIXD studies on pentacene thin films, J. Am. Chem. Soc. 127 (33) (2005) 11542–11543, https://doi.org/10.1021/ja052478e10.1021/ja052478e.s001.
[32] T.V. Desai, A.R. Woll, F. Schreiber, J.R. Engstrom, Nucleation and growth of perfluoropentacene on self-assembled monolayers: Significant changes in island density and shape with surface termination, J. Phys. Chem. C. 114 (47) (2010) 20120–20129, https://doi.org/10.1021/jp107518f.
[33] S.R. Forrest, Ultrathin organic films grown by organic molecular beam deposition and related techniques, Chem. Rev. 97 (6) (1997) 1793–1896, https://doi.org/10.1021/cr941014o.
[34] S. Kowarik, A. Gerlach, F. Schreiber, Organic molecular beam deposition: fundamentals, growth dynamics, and in situ studies, J. Phys. Condens. Matter. 20 (18) (2008) 184005, https://doi.org/10.1088/0953-8984/20/18/184005.
[35] F. Schreiber, Organic molecular beam deposition: Growth studies beyond the first monolayer, Phys. Status Solidi Appl. Res. 201 (6) (2004) 1037–1054.
[36] E. Mete, I. Demiroğlu, E. Albayrak, G. Bracco, Ş. Ellialtıoğlu, M.F. Danışman, Influence of steps on the tilting and adsorption dynamics of ordered pentacene films on vicinal Ag(111) surfaces, J. Phys. Chem. C. 116 (36) (2012) 19429–19433, https://doi.org/10.1021/jp306463w.
[37] L. Casalis, M.F. Danisman, B. Nickel, G. Bracco, T. Toccoli, S. Iannotta, G. Scoles, Hyperthermal Molecular Beam Deposition of Highly Ordered Organic Thin Films, Phys. Rev. Lett. 90 (2003) 4, https://doi.org/10.1103/PhysRevLett.90.206101.
[38] M.F. Danışman, L. Casalis, G. Scoles, Supersonic molecular beam deposition of pentacene thin films on two Ag(111) surfaces with different step densities, Phys. Rev. B. 72 (2005), 085404, https://doi.org/10.1103/PhysRevB.72.085404.
[39] T. Toccoli, A. Pallaoro, N. Coppedè, S. Iannotta, F. De Angelis, L. Mariucci, G. Fortunato, Controlling field-effect mobility in pentacene-based transistors by supersonic molecular-beam deposition, Appl. Phys. Lett. 88 (13) (2006) 132106, https://doi.org/10.1063/1.2187494.
[40] A. Yavuz, M.F. Danışman, Study on the Effect of Chemically Different Substrates on Nucleation and Growth Mechanism of Perfluoropentacene Thin Films, J. Phys. Chem. C. 123 (32) (2019) 19610–19618, https://doi.org/10.1021/acs.jpcc.9b04850.
[41] K. Fujii, C. Himcinschi, M. Toader, S. Kera, D.R.T. Zahn, N. Ueno, Vibrational properties of perfluoropentacene thin film, J. Electron Spectros. Relat. Phenomena. 174 (1-3) (2009) 65–69, https://doi.org/10.1016/j.elspec.2009.01.002.
[42] T. Breuer, M.A. Celik, P. Jakob, R. Tonner, G. Witte, Vibrational Davydov splittings and collective mode polarizations in oriented organic semiconductor crystals, J. Phys. Chem. C. 116 (27) (2012) 14491–14503, https://doi.org/10.1021/jp304080g.
[43] A. Yavuz, N. Sohrabnia, A. Yilmaz, M.F. Danışman, Mixed carboranethiol self-assembled monolayers on gold surfaces, Appl. Surf. Sci. 413 (2017) 233–241, https://doi.org/10.1016/j.apsusc.2017.03.294.
[44] E. Albayrak, M.F. Danişman, Helium diffraction study of pentacene films on Au(1 1 1), Appl. Surf. Sci. 295 (2014) 54–58, https://doi.org/10.1016/j.apsusc.2014.01.003.
[45] T. Breuer, G. Witte, Thermally activated intermixture in pentacene-perfluoropentacene heterostructures, J. Chem. Phys. 138 (11) (2013) 114901, https://doi.org/10.1063/1.4795004.
[46] F.-J. Meyer zu Heringdorf, M.C. Reuter, R.M. Tromp, The nucleation of pentacene thin films, Appl. Phys. A Mater. Sci. Process. 78 (6) (2004) 787–791, https://doi.org/10.1007/s00339-003-2432-x.
[47] A. Winkler, On the nucleation and initial film growth of rod-like organic molecules, Surf. Sci. 652 (2016) 367–377, https://doi.org/10.1016/j.susc.2016.02.015.
[48] S. Pratontep, M. Brinkmann, F. Nüesch, L. Zuppiroli, Nucleation and growth of ultrathin pentacene films on silicon dioxide: Effect of deposition rate and substrate temperature, Synth. Met. 146 (3) (2004) 387–391, https://doi.org/10.1016/j.synthmet.2004.08.017.
[49] J. Libuda, H.-J. Freund, Molecular beam experiments on model catalysts, Surf. Sci. Rep. 57 (7-8) (2005) 157–298, https://doi.org/10.1016/j.surfrep.2005.03.002.
[50] I. Salzmann, S. Duhm, G. Heimel, M. Oehzelt, R. Kniprath, R.L. Johnson, J.P. Rabe, N. Koch, Tuning the ionization energy of organic semiconductor films: The role of intramolecular polar bonds, J. Am. Chem. Soc. 130 (39) (2008) 12870–12871, https://doi.org/10.1021/ja804793a.
[51] N.M. Kreienborg, C. Merten, How to treat C-F stretching vibrations? A vibrational CD study on chiral fluorinated molecules, Phys. Chem. Chem. Phys. 21 (7) (2019) 3506–3511.